Model Hamiltonian for Altermagnetic Topological Insulators

Rafael González-Hernández[1, *] and Bernardo Uribe[2, †]

[1]*Departamento de Física y Geociencias, Universidad del Norte,*
Km. 5 Vía Antigua Puerto Colombia, Barranquilla 081007, Colombia
[2]*Departamento de Matemáticas y Estadística, Universidad del Norte,*
Km. 5 Vía Antigua Puerto Colombia, Barranquilla 081007, Colombia
(Dated: August 1, 2025)

We present models of topological insulating Hamiltonians exhibiting intrinsic altermagnetic features, protected by combined three-fold or four-fold rotational symmetries with time-reversal. We demonstrate that the spin Chern number serves as a robust topological invariant in two-dimensional systems, while for three-dimensional structures, the topological nature is characterized by the spin Chern numbers computed on the $k_z=0$ and $k_z=\pi$ planes. The resulting phases support symmetry-protected boundary modes, including corner, hinges and surface states, whose structure is determined by the magnetic symmetry and the local magnetic moments. Our findings bridge the fields of altermagnetism and topological quantum matter, and establish a theoretical framework for engineering spintronic topological systems without net magnetization.

INTRODUCTION

Altermagnetism has recently emerged as a distinct class of collinear magnetic order, complementing the conventional paradigms of ferromagnetism and antiferromagnetism. Unlike ferromagnets, which exhibit a net magnetization, or conventional antiferromagnets, where the electronic structure remains spin-degenerate throughout the entire Brillouin zone, altermagnets combine zero net magnetic moment with a momentum-dependent spin splitting of the electronic bands.[1–6] Such unconventional behavior originates from a symmetry-enforced breaking of Kramers degeneracy. This is enabled by a time-reversal symmetry breaking, together with the presence of a combination of specific crystalline symmetries, such as rotations or rotoinversions, with time reversal symmetry, thus connecting magnetic sublattices with opposite spin orientation. This momentum-space spin splitting occurs without spin-orbit coupling and it is symmetry-protected, distinguishing altermagnets from both traditional magnetic systems and spin–orbit band splitting.[7–10] Recent experimental studies have provided a clear evidence for such behavior in candidate materials, as MnTe,[11–14] CrSb[15–18] and Mn_5Si_3,[19–22] confirming the theoretical predictions and establishing altermagnetism as a viable platform for spintronic applications.

On the other hand, the study of topological phases of matter has transformed our understanding of quantum materials.[23–26] Topological insulators (TIs), characterized by insulating bulk bands and robust gapless boundary states, are classified by quantized topological invariants such as the $\mathbb{Z}_2$ index or the spin Chern number.[27–35] These phases also support dissipationless edge or surface transport channels. The intersection of altermagnetism and topology represents a rapidly developing area of research. Altermagnets, with their intrinsic spin-split bands and time-reversal symmetry breaking, offer a natural foundation for realizing topological phases with unconventional spin textures and protected edge states.[36–43] In particular, symmetry operations of the form $\mathcal{C}_l\mathbb{T}$, where $\mathcal{C}_l$ is an l-fold rotation and $\mathbb{T}$ denotes time-reversal symmetry, can stabilize topological band structures with altermagnetic character. While previous models have focused on metallic systems featuring nodal lines or Weyl points protected by magnetic symmetries,[44–51] the realization of fully gapped 3D topological altermagnets remains an open challenge. Engineering tight-binding models or materials that combine the $\mathcal{C}_l\mathbb{T}$ magnetic symmetries with a bulk band gap is thus a key goal for advancing both theoretical understanding and experimental discovery.

In this work, we present a framework for engineering two-dimensional (2D) and three-dimensional (3D) topological insulator Hamiltonians that exhibit altermagnetic behavior. The approach begins by designing a spin-up sector Hamiltonian with a non-zero Chern number and $(\mathcal{C}_l)^2$ symmetry. A full 4×4 Hamiltonian is then constructed adjoining a spin-down sector preserving the full $\mathcal{C}_l\mathbb{T}$ symmetry, resulting in spin-resolved bands with distinct energies while ensuring an odd spin Chern number to retain the topological insulating phase. The 3D Hamiltonian is constructed by adding an off-diagonal term which keeps the Hamiltonian gapped and intertwines the a trivial 2D Hamiltonian with a 2D TI Hamiltonian in differents k_z-planes.

We specifically analyze two symmetry cases: $\mathcal{C}_{4z}\mathbb{T}$ and $\mathcal{C}_{3z}\mathbb{T}$, corresponding to d-wave and f-wave altermagnetic states respectively. For each case, we provide model Hamiltonians, explore their electronic band structures, spin textures in momentum space, edge-state spectra in real space, and topological phase diagrams using the spin Chern number as the defining invariant. These constructions not only elucidate the symmetry principles governing topological altermagnetic phases but also serve as a signal for material realizations in cases such as FeSe,

* rhernandezj@uninorte.edu.co
† bjongbloed@uninorte.edu.co

where the interplay of symmetry, topology and magnetism could lead to discover novel quantum phases.

I. ENGINEERING TI ALTERMAGNETIC HAMILTONIANS

A. 2D Hamiltonians

There is a procedure to engineer an 4×4 TI Hamiltonian with altermagnetic features. The altermagnetic structure can be obtained whenever an l-fold rotation $\mathcal{C}_l$ composed with time reversal $\mathbb{T}$ is enforced on a Hamiltonian and its eigenstates are not degenerate. The topological insulating feature is enforced if the spin Chern number (SCN) is odd.

We start with a 2×2 gapped Hamiltonian whose Chern number is ±1 and which preserves the symmetry $(\mathcal{C}_l\mathbb{T})^2 = -(\mathcal{C}_l)^2$. This Hamiltonian will be modelling the spin up eigenstates and will be denoted as follows:

$$H^\uparrow(\mathbf{k}) = \begin{pmatrix} M^\uparrow(\mathbf{k}) & A^\uparrow(\mathbf{k}) \\ A^\uparrow(\mathbf{k})^* & -M^\uparrow(\mathbf{k}) \end{pmatrix}. \quad (1)$$

The Hamiltonian preserves the $(\mathcal{C}_l\mathbb{T})^2$ symmetry if

$$(\mathcal{C}_l)^2 H^\uparrow(\mathbf{k})(\mathcal{C}_l)^{-2} = H^\uparrow((\mathcal{C}_l)^2\mathbf{k}) \quad (2)$$

where $\mathcal{C}_l$ is the diagonal matrix $\mathcal{C}_l = \text{diag}(e^{\frac{2\pi i}{l}}, e^{-\frac{2\pi i}{l}})$. The topological insulating feature of $H^\uparrow$ can be secured if we choose a variant of the BHZ Hamiltonian for each value of $l \in \{3,4\}$.

Define the 4×4 Hamiltonian

$$H(\mathbf{k}) = \begin{pmatrix} H^\uparrow(\mathbf{k}) & \\ & H^\downarrow(\mathbf{k}) \end{pmatrix} \quad (3)$$

where $H^\downarrow(\mathbf{k})$ is defined by the equation

$$H^\downarrow(\mathbf{k}) = \mathcal{C}_l \left(H^\uparrow(\mathcal{C}_l\mathbb{T}\mathbf{k})\right)^* \mathcal{C}_l^{-1} \quad (4)$$

and assign to the operators $\mathbb{T}$ and $\mathcal{C}_l$ the 4×4 matrices

$$\mathbb{T} \mapsto \begin{pmatrix} 0 & \mathrm{I}_2 \\ -\mathrm{I}_2 & 0 \end{pmatrix}\mathbb{K} \text{ and } \mathcal{C}_l \mapsto \begin{pmatrix} \mathcal{C}_l & 0 \\ 0 & \mathcal{C}_l^{-1} \end{pmatrix} \quad (5)$$

respectively. The Hamiltonian $H(\mathbf{k})$ is built to preserve the symmetry $\mathcal{C}_l\mathbb{T}$, which in equations is the following,

$$(\mathcal{C}_l\mathbb{T})H(\mathbf{k})(\mathcal{C}_l\mathbb{T})^{-1} = H(\mathcal{C}_l\mathbb{T}\mathbf{k}), \quad (6)$$

and this equation is satisified if and only if Eqns. (2) and (4) are satisfied. Therefore we just need to check Eqn. (2) for the 2×2 Hamiltonian $H^\uparrow$ and Eqn. (4) specifies how to construct the Hamiltonian $H^\downarrow$.

Here the spin z matrix S_z is the diagonal matrix $S_z = \text{diag}(1,1-1-1)$ and it commutes with the Hamiltonian $H(\mathbf{k})$.

If $E_0^\uparrow(\mathbf{k})$ and $E_0^\downarrow(\mathbf{k})$ are the negative energies of the Hamiltonians $H^\uparrow$ and $H^\downarrow$ respectively, we know from

Eqn. (4) that $E_0^\uparrow(\mathbf{k}) = E_0^\downarrow(\mathcal{C}_l\mathbb{T}\mathbf{k})$. The altermagnetic feature of the Hamiltonian H emerges when $H^\uparrow$ is chosen such that $E_0^\uparrow(\mathbf{k}) \neq E_0^\downarrow(\mathbf{k})$. Whenever this happens, the spin up valence eigenstate $\psi_0^\uparrow(\mathbf{k})$ has a different energy than the one of the spin down valence eigenstate $\psi_0^\downarrow(\mathbf{k})$, and the altermagnetic feature of the Hamiltonian appears.

1. $\mathcal{C}_{4z}\mathbb{T}$ symmetry

The case $l=4$ has been studied in several works with appealingly similar Hamiltonians.[35,38,52] Here we propose a very general realization of a TI Altermagnetic Hamiltonian with $\mathcal{C}_{4z}\mathbb{T}$ symmetry which incorporates the parameters of Hamiltonians appearing in previous works.[35,38,52]

Consider the Hamiltonian $H_4^\uparrow(\mathbf{k})$ of BHZ[53] type with:

$$M_4^\uparrow(\mathbf{k}) = M_0 - K_1\cos(k_x) - K_2\cos(k_y), \quad (7)$$
$$A_4^\uparrow(\mathbf{k}) = G_1\sin(k_x) + iG_2\sin(k_y), \quad (8)$$

where K_1, K_2, G_1, G_2 are non-zero real parameters. Whenever $K_i=1=G_i$ we obtain the BHZ Hamiltonian which is gapless for $M_0 \in \{-2,0,2\}$ and whose Chern number is

$$c_1 = \begin{cases} 0 & \text{for} & |M_0| > 2 \\ -1 & \text{for} & 0 < M_0 < 2 \\ 1 & \text{for} & -2 < M_0 < 0. \end{cases} \quad (9)$$

The $(\mathcal{C}_{4z})^2 = \mathcal{C}_{2z}$ action on momentum coordinates is $\mathcal{C}_{2z}(k_x,k_y)=(-k_x,-k_y)$ and the 2×2 associated matrix is $\text{diag}(i,-i)$. Eqn. (2) is satisfied because of the following identities:

$$(\mathcal{C}_{4z})^2 H_4^\uparrow(\mathbf{k})(\mathcal{C}_{4z})^{-2} = \text{diag}(i,-i)H_4^\uparrow(\mathbf{k})\text{diag}(-i,i) \quad (10)$$
$$= H_4^\uparrow(-\mathbf{k}) \quad (11)$$
$$= H_4^\uparrow((\mathcal{C}_{4z})^2\mathbf{k}). \quad (12)$$

Since $\mathcal{C}_{4z}\mathbb{T}(k_x,k_y) = (k_y,-k_x)$, Eqn. (4) reads

$$H_4^\downarrow(k_x,k_y) = \quad (13)$$
$$\text{diag}(\tfrac{1+i}{\sqrt{2}},\tfrac{1-i}{\sqrt{2}})\left(H_4^\uparrow(k_y,-k_x)\right)^*\text{diag}(\tfrac{1-i}{\sqrt{2}},\tfrac{1+i}{\sqrt{2}}) \quad (14)$$

which implies that

$$M_4^\downarrow(\mathbf{k}) = M_0 - K_1\cos(k_y) - K_2\cos(k_x), \quad (15)$$
$$A_4^\downarrow(\mathbf{k}) = iA_4^\downarrow(k_y,-k_x)^* \quad (16)$$
$$= -G_2\sin(k_x) + iG_1\sin(k_y). \quad (17)$$

The 4×4 Hamiltonian

$$H_4(\mathbf{k}) = \begin{pmatrix} H_4^\uparrow(\mathbf{k}) & \\ & H_4^\downarrow(\mathbf{k}) \end{pmatrix} \quad (18)$$

preserves inversion symmetry P, which is equivalent to $\mathcal{C}_{2z}$ in two-dimensions, breaks times reversal symmetry

and preserves the combination $\mathcal{C}_{4z}\mathbb{T}$ with associated matrix the product

$$\mathcal{C}_{4z}\mathbb{T} \mapsto \begin{pmatrix} \mathcal{C}_{4z} & \\ & \mathcal{C}_{4z}^{-1} \end{pmatrix} \begin{pmatrix} 0 & \mathrm{I}_2 \\ -\mathrm{I}_2 & 0 \end{pmatrix} \mathbb{K} \qquad (19)$$

where $\mathrm{diag}(\frac{1+i}{\sqrt{2}}, \frac{1-i}{\sqrt{2}})$ is the matrix associated to $\mathcal{C}_{4z}$.

Fig. 1 a) illustrates the tight-binding model of a 2D altermagnetic phase on a square lattice, characterized by $\mathcal{C}_{4z}\mathbb{T}$ symmetry. The term M_0 serves as a mass term, capturing the asymmetry between the two sublattice atoms due to opposite local magnetizations that cancel out in total. The model includes the hopping parameters: K_1 and K_2 denote intra-orbital (s–s and p–p) up-channel hoppings along the x and y directions, respectively, while G_1 and G_2 correspond to inter-orbital (s–p) up-channel hoppings along the same directions. For the down-channel hoppings, the K_1 and K_2 (G_1 and G_2) are established for the y and x directions as it is defined in the Eqn. (18). These hopping terms define the momentum-dependent spin interactions that break time-reversal symmetry in the 2D square system. All hopping amplitudes and energy parameters presented in this work are in units of eV.

For the $\mathcal{C}_{4z}\mathbb{T}$-symmetric Hamiltonian given in Eqn. (18), the energies of the spin-resolved valence band eigenstates are expressed as

$$E_0^{\uparrow} = -\sqrt{(M^{\uparrow})^2 + |A^{\uparrow}|^2}, \qquad (20)$$

$$E_0^{\downarrow} = -\sqrt{(M^{\downarrow})^2 + |A^{\downarrow}|^2}, \qquad (21)$$

Notably, along the high-symmetry directions where $k_x = \pm k_y$, one finds $E_0^{\uparrow}(\mathbf{k}) = E_0^{\downarrow}(\mathbf{k})$, reflecting the symmetry-enforced degeneracy dictated by the underlying $\mathcal{C}_{4z}\mathbb{T}$ invariance.

Fig. 1 b) presents the spin-resolved band structure calculated for representative parameters: $M_0=1$, $K_1=2.125$, $K_2 = \frac{1}{K_1}$, $G_1=1.75$, and $G_2 = \frac{1}{G_1}$. The energy bands exhibits a momentum-dependent spin splitting induced by orbital hopping asymmetry, which reverses the spin energy band sign between the Γ–X and Γ–Y directions. In addition, a nodal line emerges along the Γ–M path, indicating symmetry-protected band crossings characteristic of the model.[38,44]

In the case that $K_1=K_2$, that is when the altermagnetic interaction is due only to the inter-orbital hopping parameters $G_1 \neq G_2$, we have that $E_0^{\uparrow}=E_0^{\downarrow}$ implies the equation $|A^{\uparrow}|=|A^{\downarrow}|$, and this one leads to $\sin(k_x)=\pm \sin(k_y)$. This happens whenever $k_x=\pm k_y$ or $k_x=\pi \pm k_y$.

This alternating spin polarization across momentum space is a hallmark of $\mathcal{C}_{4z}\mathbb{T}$-symmetric altermagnetism.

In the case that $G_1 = G_2$, the equation $E_0^{\uparrow} = E_0^{\downarrow}$ implies that $(M^{\uparrow})^2 - (M^{\downarrow})^2 = 0$ and this implies that either $M^{\uparrow} = M^{\downarrow}$ or $M^{\uparrow} + M^{\downarrow} = 0$. The first equation replicates the equation $k_x = \pm k_y$, while the second implies

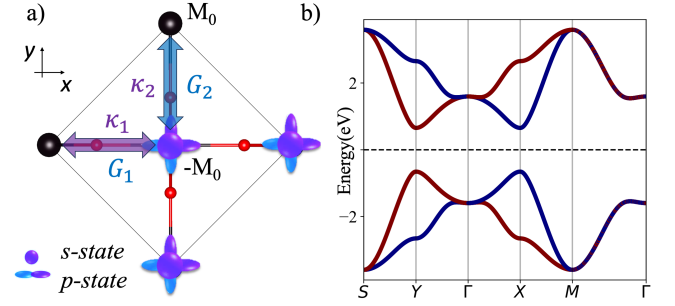FIG. 1. (a) Schematic representation of a two-dimensional $\mathcal{C}_{4z}\mathbb{T}$-symmetric altermagnetic system on an square lattice. The diagram illustrates the tight-binding model and hopping parameters, where arrows indicate the hopping interactions. The mass term M_0 captures the sublattice asymmetry arising from oppositely aligned local magnetizations. K_1 and K_2 denote the intra-site hoppings between orbitals (s–s and p–p) along the x- and y-directions, respectively. G_1 and G_2 represent the inter-site hoppings (between s and p orbitals) along x and y, respectively, as defined in the Hamiltonian in Eqn. (18). (b) Spin-resolved band structure for the altermagnetic model, with parameters set to $M_0 = 1$, $K_1= 2.125$, $K_2=\frac{1}{K_1}$, $G_1 = 1.75$, and $G_2=\frac{1}{G_1}$. All parameters are given in eV. Time-reversal symmetry breaking leads to opposite spin splitting of the bands along the Γ–X and Γ–Y paths.

the equation

$$\cos(k_x) + \cos(k_y) = \frac{2M_0}{K_1+K_2}. \qquad (22)$$

This equation has solutions whenever $|M_0| < |K_1 + K_2|$ and this is exactly when the Hamiltonian H_4 has topological insulating features. In Fig. 6 c) we see the spin texture of the upper valence band and the inner ring of change of spin, similar to the one described the solution of the Eqn. (22).

In order to avoid the inner rings or the extra lines $k_x=\pi \pm k_y$ in the spin texture of the upper valence band in H_4, we need to take $K_1 \neq K_2$ and $G_1 \neq G_2$ as in Fig. 2 c).

We note here that whenever $K_2 = 2-K_1$ and $G_1 = G_2$ the diagonal term $M_4^{\uparrow}$ can be written as the standard term in the BHZ Hamiltonian

$$M := M_0 - \cos(k_x) - \cos(k_y) \qquad (23)$$

plus a an altermagnetic J-term

$$J := (1 - K_1)\left(\cos(k_x) - \cos(k_y)\right) \qquad (24)$$

thus having

$$M_4^{\uparrow} = M + J \quad \text{and} \quad M_4^{\downarrow} = M - J. \qquad (25)$$

If the off diagonal term is

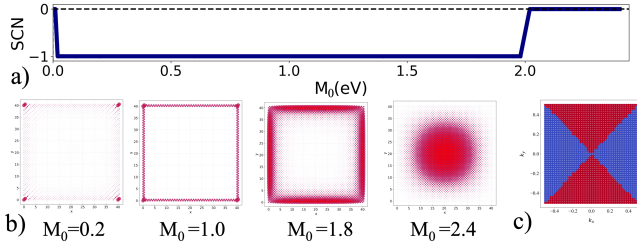$$A = G_1(\sin(k_x) + i\sin(k_y)) \qquad (26)$$

FIG. 2. Hamiltonian H_4 of Eqn. (18) fixing constants $K_1=G_1=1.01$ with $K_2=\frac{1}{K_1}$, $G_2=\frac{1}{G_1}$ and varying M_0. a) is the spin$_z$ Chern number with respect to M_0, b) are the edge states $(|\psi_n(r)|^2)$ for $M_0 \in \{0.2, 1, 1.8, 2.4\}$ and c) is the spin$_z$ texture of the upper valence band for the four values of M_0 (it is the same texture for the four cases). The Hamiltonian models a TI for $0 < |M_0| < 2$, as the spin Chern number evidences, and the local charge density of the first three phases exhibit the localization on the boundary.

the 4×4 Hamiltonian H_4 becomes the following matrix:

$$
\begin{pmatrix}
M+J & A & & \\
A^* & -M-J & & \\
& & M-J & -A^* \\
& & -A & -M+J
\end{pmatrix}. \quad (27)
$$

This is the Hamiltonian that has been used in several works that study altermagnetism in Hamiltonians that preserve the $\mathcal{C}_{4z}\mathbb{T}$ symmetry.[35,38,45] Whenever $J = 0$ this is the original BHZ Hamiltonian.[53]

The Hamiltonian H_4 of (18) with $K_1=K_2=G_1=G_2=1$ has for spin Chern number SCN $= \frac{1}{2}(c_1^\uparrow - c_1^\downarrow)$ (with $c_1^{\uparrow\downarrow}$ the Chern number of the spin up and down valence bands) the following numbers:

$$
\text{SCN} = \begin{cases} 0 & \text{for} \quad 2 < |M_0| \\ -1 & \text{for} \quad 0 < M_0 < 2 \\ 1 & \text{for} \quad -2 < M_0 < 0. \end{cases} \quad (28)
$$

Therefore we will make the choice of taking

$$
K_2 = \frac{1}{K_1}, \quad G_2 = \frac{1}{G_1}, \quad (29)
$$

and both K_1 and G_1 close to 1.

Figure 2 a) presents the phase diagram of the $\mathcal{C}_{4z}\mathbb{T}$-symmetric Hamiltonian defined in Eqn. (18), where the SCN is plotted as a function of the M_0 parameter (related with the local magnetic moment). The SCN was calculated using the computational setup detailed in our previous work[33] Topological phase transition are observed around $M_0=2$, where the SCN changes from -1 (nontrivial phase) to 0 (trivial phase), and around $M_0=0$ where the SCN changes from -1 to 1. Figure 2 b) shows the real-space probability densities of the four edge-states closest to the Fermi level in a cubic geometry for the M_0 parameters: 0.2, 1.0, 1.8, and 2.4. Boundary states were calculated in a square geometry consists of 35×35 unit cells. It is noted a transition from strongly localized corner states at $M_0=0.2$, to surface-edge states at

$M_0=1.0$ and 1.8, and finally to a trivial insulating phase at $M_0=2.4$, where the four states nearest the Fermi level become delocalized in the bulk. These edge states are in agreement with previously reported cases.[52] Figure 2 c) shows the spin texture of the top valence band across the Brillouin zone. This texture is independent of M_0, and exhibits the $\mathcal{C}_{4z}\mathbb{T}$-symmetric shape of the Hamiltonian in Eqn. (18). Both, the momentum-space spin texture and the real-space edge-state reflect the $\mathcal{C}_{4z}\mathbb{T}$ symmetry, show the features of a d-wave altermagnetic topological phase.

2. $\mathcal{C}_{3z}\mathbb{T}$ symmetry

The case $l=3$ requires first the construction of a Hamiltonian which preserves the $(\mathcal{C}_{3z})^2$ symmetry of Eqn. (2), which in this case it is equivalent to preserving the symmetry $\mathcal{C}_{3z}$ itself. Define the following terms:

$$
M_3^\uparrow = M_0 - B_0 \left(\cos(k_y) + \cos(\frac{\sqrt{3}k_x - k_y}{2}) + \cos(\frac{-\sqrt{3}k_x - k_y}{2}) \right) \quad (30)
$$

$$
J_3^\uparrow = J_0 \left(\sin(k_x) \sin(\frac{\sqrt{3}k_y - k_x}{2}) \sin(\frac{-\sqrt{3}k_y - k_x}{2}) \right) \quad (31)
$$

$$
A_3^\uparrow = A_0 \left(\sin(k_x) + \lambda \sin(\frac{\sqrt{3}k_y - k_x}{2}) + \lambda^2 \sin(\frac{-\sqrt{3}k_y - k_x}{2}) \right) \quad (32)
$$

with $\lambda = e^{\frac{2\pi i}{3}}$, and define the spin up hamiltonian $H_3^\uparrow(\mathbf{k})$ as follows:

$$
H_3^\uparrow = \begin{pmatrix} M_3^\uparrow + J_3^\uparrow & A_3^\uparrow \\ (A_3^\uparrow)^* & -M_3^\uparrow - J_3^\uparrow \end{pmatrix}. \quad (33)
$$

In momentum coordinates the C_3 rotation is as follows

$$
\mathcal{C}_{3z}(k_x, k_y) = (\frac{-k_x - \sqrt{3}k_y}{2}, \frac{\sqrt{3}k_x - k_y}{2}) \quad (34)
$$

and as a representation we associate to $\mathcal{C}_{3z}$ the matrix $\text{diag}(\sigma, \sigma^{-1})$ where $\sigma = e^{\frac{2\pi i}{6}}$ with $\sigma^2 = \lambda$.

Calculating $A_3^\uparrow(\mathcal{C}_{3z}\mathbf{k})$ we get the equation

$$
A_3^\uparrow(\mathcal{C}_{3z}\mathbf{k}) = \lambda A_3^\uparrow(\mathbf{k}), \quad (35)
$$

which implies the matrix equation

$$
\text{diag}(\sigma, \sigma^{-1}) H_3^\uparrow(\mathbf{k}) \text{diag}(\sigma^{-1}, \sigma) = H_3^\uparrow(\mathcal{C}_{3z}\mathbf{k}) \quad (36)
$$

thus implying Eqn. (2) when applied twice.

The Hamiltonian $H_3^\downarrow(\mathbf{k})$ is defined following Eqn. (4)

$$
H_3^\downarrow(\mathbf{k}) := \text{diag}(\sigma, \sigma^{-1}) H_3^\uparrow(-\mathcal{C}_{3z}\mathbf{k}) \text{diag}(\sigma^{-1}, \sigma) \quad (37)
$$

implying that

$$
M_3^\downarrow(\mathbf{k}) := M_3^\uparrow(-\mathcal{C}_{3z}\mathbf{k}) = M_3^\uparrow(\mathbf{k}), \quad (38)
$$

$$
J_3^\downarrow(\mathbf{k}) := J_3^\uparrow(-\mathcal{C}_{3z}\mathbf{k}) = -J_3^\uparrow(\mathbf{k}), \quad (39)
$$

$$
A_3^\downarrow(\mathbf{k}) := \lambda A_3^\uparrow(-\mathcal{C}_{3z}\mathbf{k})^* = -\lambda(\lambda A_3^\uparrow(\mathbf{k}))^* = -A_3^\uparrow(\mathbf{k})^*. \quad (40)
$$

The 4×4 Hamiltonian H_3 written in terms of $M^\uparrow$, $J^\uparrow$ and $A^\uparrow$ is as follows:

$$H_3(\mathbf{k}) = \begin{pmatrix} M_3^\uparrow + J_3^\uparrow & A_3^\uparrow & & \\ (A_3^\uparrow)^* & -M_3^\uparrow - J_3^\uparrow & & \\ & & M_3^\uparrow - J^\uparrow & -(A_3^\uparrow)^* \\ & & -A_3^\uparrow & -M_3^\uparrow + J_3^\uparrow \end{pmatrix}. \tag{41}$$

The energies of the valence spin up and spin down eigenstates are respectively

$$E_0^\uparrow = -\sqrt{(M_3^\uparrow + J_3^\uparrow)^2 + |A_3^\uparrow|^2}, \tag{42}$$

$$E_0^\downarrow = -\sqrt{(M_3^\uparrow - J_3^\uparrow)^2 + |A_3^\uparrow|^2} \tag{43}$$

and the energies are equal whenever $M^\uparrow=0$ or $J^\uparrow=0$. The second equation implies that $k_x=0$ or $k_x=\pm\sqrt{3}k_y$, which is a triangular tesselation of the momentum space, and the first implies the equation

$$\cos(k_y) + \cos(\frac{\sqrt{3}k_x - k_y}{2}) + \cos(\frac{-\sqrt{3}k_x - k_y}{2}) = \frac{M_0}{B_0} \tag{44}$$

which has solutions only when $\left|\frac{M_0}{B_0}\right| < 3$. Since H_3 is precisely TI whenever $\left|\frac{M_0}{B_0}\right| < 3$, we see that the appearance of a nodal line in the Hamiltonian is unavoidable for the TI phase. This nodal line looks like a circle around the Γ point and can be appreciated in Fig. 3 b) where it induces a change of spin the texture around Γ.

Since we can scale all constants of the Hamiltonian at the same time, we will choose

$$B_0 = \frac{2}{3} \tag{45}$$

for the relevant values of M_0 be the same as in the case of the Hamiltonian H_4 of Eqn. (18). The constants J_0 and A_0 will be close to 0 and 1 respectively, and whenever $J_0=0$ and $A_0=1$ the Hamiltonian H_3 is gapless for $M_0 \in \{-2, 0, 2\}$ and the SCN of the valence bands is

$$\text{SCN} = \begin{cases} 0 & \text{for} \quad 2 < |M_0| \\ -1 & \text{for} \quad 0 < |M_0| < 2. \end{cases} \tag{46}$$

Note that the SCN is only -1 because the Hamiltonian $H_3^\uparrow$ has Chern number -1 for $0 < |M_0| < 2$. This case differs from the Hamiltonian H_4 where the SCN changes from -1 to 1 on $M_0=0$ as it is shown in Eqn. (28) and illustrated in Fig. 2.

Figure 3 a) illustrates the topological phase transition in the $\mathcal{C}_{3z}\mathbb{T}$-symmetric model described by Eqn. (41), controlled by the onsite mass term M_0. A transition from a nontrivial (SCN=1) to a trivial (SCN=0) phase occurs near $M_0=2$. This transition highlights the tunability of the topological phase with the compensate local magnetization of the opposite atomic sublattices, described in the M_0 value. The quantized SCN=1 reflects a robust topological invariant,[31] in agreement with the topological classification of 2D-systems preserving combined $\mathcal{C}_{3z}\mathbb{T}$ symmetry.
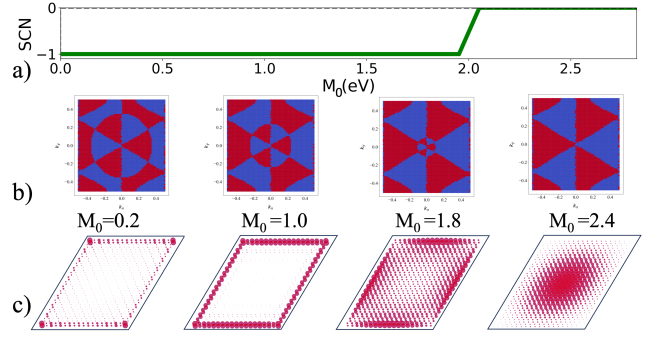

FIG. 3. (a) Phase diagram of the $\mathcal{C}_{3z}\mathbb{T}$-symmetric altermagnetic model described by Eqn. (41), showing the SCN as a function of the mass term M_0. A topological phase transition occurs near $M_0=2$. (b) Spin-projected states of the top valence band across the Brillouin zone, and (c) Spin-resolved edge states for a finite system, calculated at $M_0 = 0.2$, 1.0, 1.8, and 2.4, with fixed parameters $A_0=1.01$, $B_0=2/3$ and $J_0=0.01$. The spin textures exhibit an f-wave AM type characteristic of the $\mathcal{C}_{3z}\mathbb{T}$ symmetry, with a nodal ring whose radius decreases as M_0 increases. Both the spin textures and edge-state distributions manifest the $\mathcal{C}_{3z}\mathbb{T}$ symmetry of the Hamiltonian in Eqn. (41).

Figure 3 b) and 3 c) display the spin texture on the top valence band across the Brillouin zone and the corresponding spin-resolved edge-state spectra for a finite sample, respectively. Boundary states were calculated in an geometry composed of 35×35 unit cells. These results are computed for $M_0 = 0.2$, 1.0, 1.8, and 2.4, with fixed parameters $A_0 = 1.01$ and $J_0 = 0.01$, representing inter-sublattice and intra-sublattice hopping amplitudes, respectively. In all cases, the spin textures reveal an f-wave altermagnetic type, which is characteristic of the $\mathcal{C}_{4z}\mathbb{T}$-protected symmetry.[2] A nodal ring centered at the Γ point where the spin texture reverses, is observed, as predicted by the Eqn. (44). Its radius progressively decreases with increasing M_0. The presence of corner and edge modes within the bulk energy gap confirms the nontrivial topology for $M_0 < 2$, while for $M_0=2.4$, the absence of edge states is an signal a trivial insulating phase.

3. Topological indicator

The Bloch bundle of the valence bands for the gapped Hamiltonians H_4 and H_3 of Eqns. (18) and (41), define elements in the Magnetic Equivariant K-theory groups[54] of the 2D torus $\mathcal{K}^0_{\mathcal{C}_{4z}\mathbb{T}}(T^2)$ and $\mathcal{K}^0_{\mathcal{C}_{3z}\mathbb{T}}(T^2)$ respectively. The bulk invariant of the K-theory group $\mathcal{K}^0_{\mathcal{C}_{4z}\mathbb{T}}(T^2)$ was shown to be $\mathbb{Z}/2$ and it was further shown that it could be measured with the value mod 2 of the SCN.[35] Similarly, the bulk invariant of the K-theory group $\mathcal{K}^0_{\mathcal{C}_{3z}\mathbb{T}}(T^2)$ is also $\mathbb{Z}/2$ and can be measured with the SCN.

Hence the SCN on the gapped Hamiltonians provides the topological bulk invariant of the system. The SCN

is invariant while the altermagnet Hamiltonians remain gapped and the symmetry $\mathcal{C}_l\mathbb{T}$ is not broken.

B. 3D Hamiltonians

The Hamiltonian in Eqn. (3) can be extended to three dimensions by incorporating an intrasublattice hopping along the z-axis and an off-diagonal k_z-dependent term that preserves the $\mathcal{C}_l\mathbb{T}$ symmetry and maintains the bulk energy gap.

One proposal for such a Hamitlonian is the following:

$$\mathcal{H}(k_x,k_y,k_z) = \begin{pmatrix} \mathcal{H}^{\uparrow}(k_x,k_y,k_z) & D_0\sin(k_z)\sigma_x \\ D_0\sin(k_z)\sigma_x & \mathcal{H}^{\downarrow}(k_x,k_y,k_z) \end{pmatrix} \quad (47)$$

where the up and down sectors of the Hamiltonian are defines as follows:

$$\mathcal{H}^{\uparrow}(k_x,k_y,k_z) := H^{\uparrow}(k_x,k_y) - \cos(k_z)\sigma_z \quad (48)$$

$$\mathcal{H}^{\downarrow}(k_x,k_y,k_z) := H^{\downarrow}(k_x,k_y) - \cos(k_z)\sigma_z \quad (49)$$

with $H^{\uparrow}(k_x,k_y)$ and $H^{\downarrow}(k_x,k_y)$ the Hamiltonians defined in Eqns. (1) and (4) respectively, σ_x and σ_y are the Pauli matrices and D_0 is a non-zero real parameter.

This Hamiltonian preserves the symmetry $\mathcal{C}_{lz}\mathbb{T}$ where $\mathcal{C}_{lz}(k_x,k_y,k_z) = (\mathcal{C}_l(k_x,k_y),k_z)$ and the matrix associated to $\mathcal{C}_{lz}\mathbb{T}$ is

$$\begin{pmatrix} \mathcal{C}_l & 0 \\ 0 & \mathcal{C}_l^{-1} \end{pmatrix}\begin{pmatrix} 0 & \mathrm{I}_2 \\ -\mathrm{I}_2 & 0 \end{pmatrix}\mathbb{K}. \quad (50)$$

The Hamiltonian is gapped as long as the Hamiltonian $\mathcal{H}^{\uparrow}(k_x,k_y,k_z)$ remains gapped for $k_z = 0$ and $k_z = \pi$.

1. $\mathcal{C}_{4z}\mathbb{T}$ symmetry

The spin up and spin down sectors of the Hamiltonian become

$$\mathcal{H}_4^{\uparrow\downarrow}(\mathbf{k}) = \begin{pmatrix} \mathcal{M}_4^{\uparrow\downarrow}(\mathbf{k}) & A_4^{\uparrow\downarrow}(\mathbf{k}) \\ A_4^{\uparrow\downarrow}(\mathbf{k})^* & -\mathcal{M}_4^{\uparrow\downarrow}(\mathbf{k}) \end{pmatrix} \quad (51)$$

where

$$\mathcal{M}_4^{\uparrow}(\mathbf{k}) = M_0 - K_1\cos(k_x) - K_2\cos(k_y) - \cos(k_z), \quad (52)$$

$$A_4^{\uparrow}(\mathbf{k}) = G_1\sin(k_x) + iG_2\sin(k_y), \quad (53)$$

$$\mathcal{M}_4^{\downarrow}(\mathbf{k}) = M_0 - K_2\cos(k_x) - K_1\cos(k_y) - \cos(k_z), \quad (54)$$

$$A_4^{\downarrow}(\mathbf{k}) = -G_2\sin(k_x) + iG_1\sin(k_y). \quad (55)$$

The 3D Hamiltonian is thus

$$\mathcal{H}_4(k_x,k_y,k_z) = \begin{pmatrix} \mathcal{H}_4^{\uparrow}(k_x,k_y,k_z) & D_0\sin(k_z)\sigma_x \\ D_0\sin(k_z)\sigma_x & \mathcal{H}_4^{\downarrow}(k_x,k_y,k_z) \end{pmatrix}, \quad (56)$$

it preserves the symmetry $\mathcal{C}_{4z}\mathbb{T}$, breaks time reversal as defined in Eqn. (5), preserves inversion symmetry and it is gapped as long as $D_0 \neq 0$.

Whenever $G_1=G_2=K_1=K_2=1$ the system looses its altermagnetic feature and is trivial for $|M_0| > 3$, strong TI for $1 < |M_0| < 3$ with two spin Weyl points in the line $k_x=0=k_y$ when M_0 is positive and two spin Weyl points in the line $k_x=\pi=k_y$ when M_0 is negative, and weak TI for $|M_0| < 1$ with four spin Weyl points, two in the line $k_x=0$, $k_y=\pi$ and two in the line $k_x=\pi$, $k_y=0$. This feature is similar to the one appearing in the 3D BHZ Hamiltonian.[33] In terms of the SCN on the planes $k_z=0$ and $k_z=\pi$ the information has been summarized in Table I.

M_0	$(-\infty,-3)$	$(-3,-1)$	$(-1,1)$	$(1,3)$	$(3,\infty)$
SCN($k_z=\pi$)	0	1	-1	0	0
SCN($k_z=0$)	0	0	1	-1	0
Top. type	Tr.	STI	WTI	STI	Tr.

TABLE I. SCN on the planes $k_z=\pi$ and $k_z=0$ of the Hamiltonian $\mathcal{H}_4$ for different values of M_0 and $G_1=G_2=K_1=K_2=1$ and $D_0=0.1$. The last row indicates its topological nature: trivial insulator (Tr.), strong TI (STI) or weak TI (WTI).

The parameters K_2 and G_2 will be chosen as in Eqn. (29) and K_1 and G_1 will be values close to 1.

In Fig.4, we present the SCN and the spin$_z$ texture of the upper valence band as a function of k_z, and the four boundary states of the 3D Hamiltonian $\mathcal{H}_4(\mathbf{k})$ defined in Eqn.(56). Here we have fixed $K_1=1.01=G_1$ and $D_0=0.1$ we have plotted the cases a) $M_0=2.1$ and b) $M_0=0.5$. The case a) is a strong TI with constant spin texture on all k_z planes, two spin Weyl points and change of SCN on the planes $k_z=0$ and $k_z=\pi$. The boundary states are localized on the faces perpendicular to the z-axis. The case b) is a weak TI with same SCN mod 2 on the planes $k_z=0$ and $k_z=\pi$, four spin Weyl points located the k_z-axis with $(k_x,k_y)=(0,\pi)$ and $(k_x,k_y)=(\pi,0)$, and spin texture which flips on the k_z plane where the spin Weyl points are located. The boundary states near the Fermi level are spatially localized at the corners of the finite cubic geometry, indicating the presence of a HOTI phase. This behavior is analogous to the corner modes protected by $\mathcal{C}_{4z}\mathbb{T}$ symmetry model reported by Schindler et $al.$[55]

The results presented in Fig. 4 show the interplay between symmetry-protected topology and spatial localization of boundary states in a $\mathcal{C}_{4z}\mathbb{T}$-symmetric system. As the mass parameter M_0 is tuned, the wavefunction states of the Hamiltonian of Eqn. (56) undergoes topological phase transitions that manifest not only through quantized spin Chern numbers but also through the real-space edge-states distribution. The corner-localized to surface states, for M_0 close to 0, reflects the bulk boundary correspondences of a HOTI system enforced by the $\mathcal{C}_{4z}\mathbb{T}$ symmetry. This behavior is consistent with previous HOTI systems with combined four-fold rotation
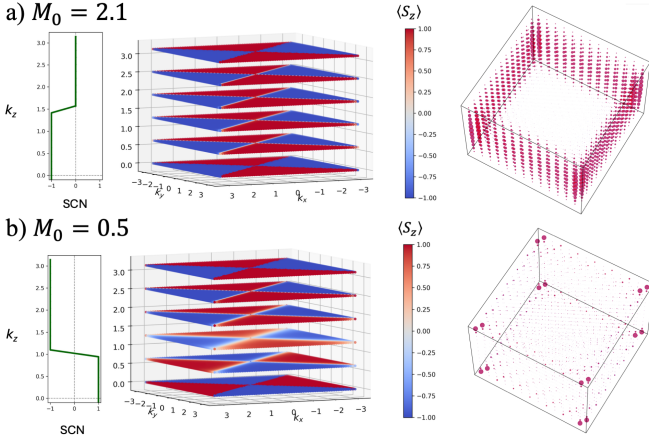
a) $M_0 = 2.1$

b) $M_0 = 0.5$

FIG. 4. $\mathcal{H}_4(\mathbf{k})$ Hamiltonian of Eqn. (56) with K_1=1.01, G_1=1.01, D_0=0.1, a) M_0=2.1 and b) M_0=0.5. The first graph is the SCN of the valence bands on planes perpendicular to the k_z-axis. The second is the spin$_z$ texture of the upper valence band on the BZ. The third are the conducting boundary states. a) is a strong TI because of the change of SCN mod 2. The SCN changes by 1 where the spin Weyl point is located, on the k_z-axis with (k_x, k_y)=(0,0). The altermagnetic feature is almost constant in all value of k_z. The edge states are localized on the faces parallel to the z-axis. b) is a weak TI because the SCN mod 2 is always 1. The SCN changes from 1 to -1 where the spin Weyl points are located, one on the k_z-axis with (k_x, k_y)=$(0,\pi)$, and the other of the k_z-axis with (k_x, k_y)=$(\pi,0)$,. The spin texture flips on the k_z locations of the spin Weyl points. The boundary states are localized in the corners, thus inducing a HOTI phase. The boundary state calculations were performed on a $13\times13\times13$ finite cubic geometry.

and time-reversal symmetry.[56,57] In addition, the surface states for M_0 close to 2 are more extended to the surface showing a strong topological insulator character, which is confirmed with the change of SCN from 0 to 1.

2. $\mathcal{C}_{3z}\mathbb{T}$ symmetry

The 3D Hamiltonian coming from the 2D Hamiltonian of Eqn. (41) is:

$$\mathcal{H}_3(\mathbf{k}) = \begin{pmatrix} \mathcal{M}_3^\uparrow + J_3^\uparrow & A_3^\uparrow & & D_0\sin(k_z) \\ (A_3^\uparrow)^* & -\mathcal{M}_3^\uparrow - J_3^\uparrow & D_0\sin(k_z) & \\ & D_0\sin(k_z) & \mathcal{M}_3^\uparrow - J^\uparrow & -(A_3^\uparrow)^* \\ D_0\sin(k_z) & & -A_3^\uparrow & -\mathcal{M}_3^\uparrow + J_3^\uparrow \end{pmatrix}$$
(57)

where

$$\mathcal{M}_3^\uparrow = M_0 - \cos(k_z) - \tag{58}$$
$$B_0\left(\cos(k_y) + \cos(\tfrac{\sqrt{3}k_x - k_y}{2}) + \cos(\tfrac{-\sqrt{3}k_x - k_y}{2})\right)$$

and $J_3^\uparrow$ and $A_3^\uparrow$ remain as in Eqns. (31) and (32).
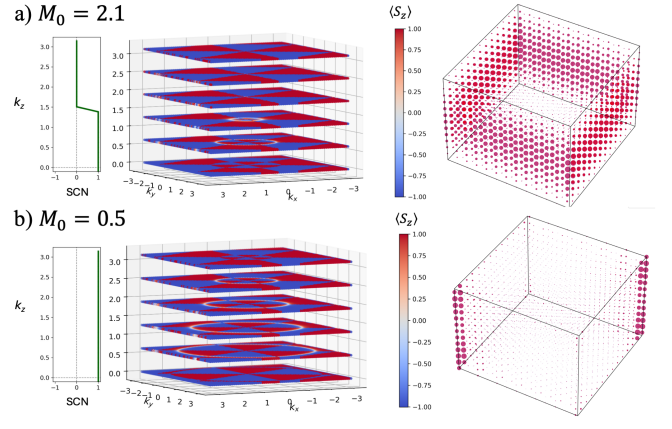

a) $M_0 = 2.1$

b) $M_0 = 0.5$

FIG. 5. $\mathcal{H}_3(\mathbf{k})$ Hamiltonian of Eqn. (57) with constants B_0=2/3, J_0=0.01, A_0=1.01, D_0=0.1, a) M_0=2.1 and b) M_0=0.5. The first graph is the SCN of the valence bands on planes perpendicular to the k_z-axis. The second is the spin$_z$ texture of the upper valence band on the BZ. The third are the conducting boundary states. a) is a strong TI because of the change of SCN mod 2. The SCN changes by 1 where the spin Weyl point is located, on the k_z-axis with (k_x, k_y)=(0,0). The altermagnetic feature is similar for all value of k_z, except when the presence of a nodal sphere makes the the spin texture to change of sign. The edge states are localized on the faces parallel to the z-axis. b) is a weak TI because the SCN is always 1. There is no change of SCN since there are no spin Weyl points. The spin texture flips sign from k_z=π to k_z=0 due to the nodal sphere present on the whole BZ. The boundary states are localized in the hinges, thus inducing a HOTI phase. Boundary states were computed using a finite cubic system of size $13\times13\times13$.

This Hamiltonian preserves the $\mathcal{C}_{3z}\mathbb{T}$ symmetry together with time reversal and breaks inversion symmetry. Whenever J_0=0 and A_0=1, this Hamiltonian is gapped as long as $M_0 \notin \{-3,-1,1,3\}$ and $D_0 \neq 0$. The SCN on the planes k_z=0 and k_z=π are as the ones of Table II and the value of M_0 determines its topological features. The altermagnetic flavour of the system is obtained when $J_0 \neq 0$.

M_0	$(-\infty, -3)$	$(-3, -1)$	$(-1, 1)$	$(1, 3)$	$(3, \infty)$
SCN(k_z=π)	0	1	1	0	0
SCN(k_z=0)	0	0	1	1	0
Top. type	Tr.	STI	WTI	STI	Tr.

TABLE II. SCN on the planes k_z=π and k_z=0 of the Hamiltonian $\mathcal{H}_3$ for different values of M_0 with J_0=0, A_0=1 and D_0=0.1. The last row indicates its topological nature: trivial insulator, strong TI or weak TI.

We have plotted in Fig. 5 the SCN with respect to k_z, the spin texture and the edge states for a) M_0=2.1 and b) M_0=0.5, fixing B_0=2/3, J_0=0.01, A_0=1.01 and D_0=0.1. The case a) is a strong TI with change of SCN from 0 in k_z=π to 1 in k_z=0, spin Weyl points localized in

the k_z-axis with $(k_x, k_y)=(0,0)$, edge states localized in the planes parallel to the z-axis, and whose spin texture changes in the presence of a nodal sphere. In contrast, case (b) corresponds to a weak TI phase, where the SCN remains constant across k_z, and no spin Weyl points are present. The system instead hosts hinge states propagating along the z-axis, accompanied by a sign reversal of the spin texture between $k_z=0$ and $k_z=\pi$. Additionally, a symmetry-protected nodal line is observed in the spin texture across varying k_z planes. These results, together with the recent discovery of floating edge bands in altermagnetic BHZ-type systems,[39] highlight the unconventional boundary phenomena that can arise in altermagnetic topological phases.

3. Topological invariants

The 3D bulk invariants of the $\mathcal{C}_{4z}\mathbb{T}$ symmetry can be determined from the Magnetic Equivariant K-theory[54] groups $\mathcal{K}^0_{\mathcal{C}_{4z}\mathbb{T}}(T^3)$ of the 3D torus T^3 (similarly for $\mathcal{C}_{3z}\mathbb{T}$).

To calculate this K-theory group we are going to use the Mayer-Vietoris sequence[54] and the information we already know from the 2D case.[35] Cover T^3 with open sets U and V where $U = T^2 \times (-\frac{3\pi}{4}, \frac{3\pi}{4})$ and $V = T^2 \times (\frac{\pi}{4}, \frac{7\pi}{4})$. The intersection $U \cap V$ is equivaraintly homotopic to the union of the planes $k_z=\frac{\pi}{2}$ and $k_z=-\frac{\pi}{2}$, U and V are equivaraintly homotopic to $k_z=0$ and $k_z=\pi$ respectively. Therefore we have the following isomorphisms:

$$\mathcal{K}^0_{\mathcal{C}_{4z}\mathbb{T}}(U) \cong \mathcal{K}^0_{\mathcal{C}_{4z}\mathbb{T}}(V) \cong \mathcal{K}^0_{\mathcal{C}_{4z}\mathbb{T}}(T^2) \qquad (59)$$

$$\mathcal{K}^0_{\mathcal{C}_{4z}\mathbb{T}}(U \cap V) \cong K^0_{\mathcal{C}_{2z}}(T^2) \qquad (60)$$

where $K^0_{\mathcal{C}_{2z}}(T^2)$ stands for the equivariant complex K-theory of the 2-fold rotation $\mathcal{C}_{2z}$ on T^2.

Since we know that $K^{-1}_{\mathcal{C}_{2z}}(T^2) = 0$,[54] and that the restriction map

$$r : \mathcal{K}^0_{\mathcal{C}_{4z}\mathbb{T}}(T^2) \to K^0_{\mathcal{C}_{2z}}(T^2) \qquad (61)$$

is injective on its torsion free part,[58] we can deduce that we have a exact sequene

$$0 \to \mathcal{K}^0_{\mathcal{C}_{4z}\mathbb{T}}(T^3) \to \mathcal{K}^0_{\mathcal{C}_{4z}\mathbb{T}}(T^2)^{\oplus 2} \to K^0_{\mathcal{C}_{2z}}(T^2) \qquad (62)$$

where the right hand side map is $a_0 \oplus a_1 \mapsto r(a_0) + r(a_1)$. We know that[35]

$$\mathcal{K}^0_{\mathcal{C}_{4z}\mathbb{T}}(T^2) \cong \mathbb{Z}^{\oplus 2} \oplus \mathbb{Z}/2 \qquad (63)$$

where the $\mathbb{Z}/2$ invariant can be obtained from the parity of the SCN. Hence we see that our desired K-theory group is:

$$\mathcal{K}^0_{\mathcal{C}_{4z}\mathbb{T}}(T^3) \cong \mathbb{Z}^{\oplus 2} \oplus \mathbb{Z}/2^{\oplus 2}, \qquad (64)$$

where the bulk invariants are precisely the two copies of $\mathbb{Z}/2$, and are measured calculating the SCN on the planes $k_z=0$ and $k_z=\pi$.

The torsion subgroup of $\mathcal{K}^0_{\mathcal{C}_{4z}\mathbb{T}}(T^3)$ which is the two copies of $\mathbb{Z}/2$ is the TI indicator for this symmetry. Exactly the same applies to $\mathcal{K}^0_{\mathcal{C}_{3z}\mathbb{T}}(T^3)$.

Therefore the four different phases that can appear are presented in Table III and are compatible with the information provided by the SCN presented in Tables I and II.

Top. type	Tr.	STI	WTI	STI
SCN($k_z=\pi$)	0	1	1	0
SCN($k_z=0$)	0	0	1	1

TABLE III. Indicators for the topological invariants appearing in the torsion subgroup of $\mathcal{K}^0_{\mathcal{C}_{4z}\mathbb{T}}(T^3)$ and $\mathcal{K}^0_{\mathcal{C}_{3z}\mathbb{T}}(T^3)$. Here the torsion subgroup consists of two copies of $\mathbb{Z}/2$, the four possibilities for the invariant apear in the table and they are obtained from the calculation of the SCN mod 2 on the planes fixed by $\mathcal{C}_{4z}\mathbb{T}$ or $\mathcal{C}_{3z}\mathbb{T}$ which are $k_z=0$ and $k_z=\pi$. If the SCN is 1 and it does not change then we are in the weak TI realm, while the change of the SCN detects the strong TI feature. The topological nature can be obtained from the information of the SCN as presented in Tables I and II.

II. MATERIAL REALIZATION

Fig. 6 presents the material realization of a 2D-dimensional topological altermagnetic phase in the FeSe monolayer, a material recently studied and known for its structural simplicity.[59–62] The FeSe monolayer has a square Bravais lattice with two Fe atoms, and two Se atoms positioned above and below the Fe plane in a layered configuration. Fig. 6 a) illustrates the schematic model of the monolayer FeSe structure, where Fe_1 and Fe_2 atoms occupy distinct sublattices with antiparallel magnetic moments. The collinear antiferromagnetic configuration of monolayer FeSe yields zero net magnetization and preserves the combined inversion and time-reversal symmetries. This $P\mathbb{T}$ symmetry ensures a Kramers degeneracy at every $\mathbf{k}$-point in the Brillouin zone.

However, FeSe monolayer may realize an altermagnetic phase through various symmetry-breaking mechanisms.[63] In particular, when grown on a substrate as $SrTiO_3$,[64,65] vertical displacements of the Se atoms break inversion symmetry, thereby lifting the $P\mathbb{T}$ degeneracy. This symmetry breaking results in momentum-dependent spin splitting as shown in Fig. 6 b). The band spin-splitting changes sign between the Γ–X and Γ–Y directions, this anisotropic spin-splitting is the signal of a d-wave altermagnetic texture. This spin anisotropy is consistent with the $\mathcal{C}_{4z}\mathbb{T}$ symmetry explored in the Hamiltonian model of Eqn. (18).

Fig. 6 c-d) confirm the altermagnetic topological nature of the FeSe material. In Fig. 6 c), the spin Hall conductivity σ^z_{xy} exhibits a quantized value at $e/4\pi$ within the bulk energy gap, indicating a nontrivial topological
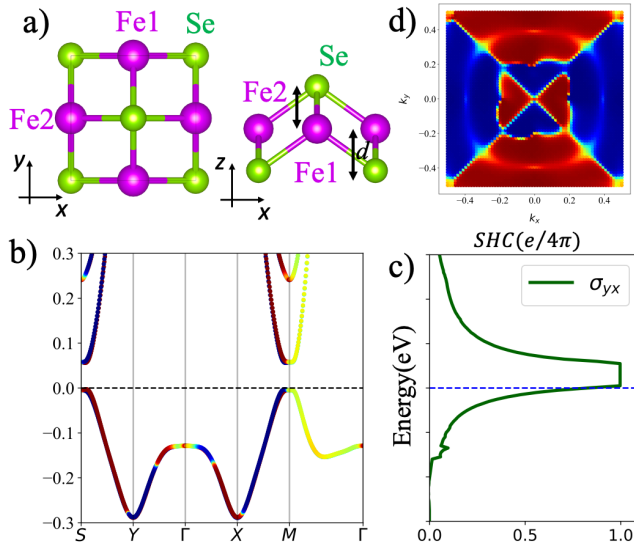
FIG. 6. Electronic and topological properties of the two-dimensional altermagnetic phase in FeSe. (a) Ball-and-stick structural model, where Fe_1 and Fe_2 atoms have opposite magnetic moments. A slight vertical displacement of the bottom Se layer breaks $P\mathbb{T}$ symmetry. (b) Spin-resolved band structure showing momentum-dependent spin splitting with opposite signs along the Γ–X and Γ–Y directions. (c) Spin Hall conductivity σ_{xy}^{z} as a function of Fermi energy, which presents a quantized value within the band gap. (d) Anisotropic d-wave spin-texture on the valence band. (e) Spin-projected surface states of the FeSe, revealing topological edge modes in the FeSe altermagnet phase.

response associated with a spin Chern number of 1. This SCN=1 was independently calculated using the Chern number for the negative spin-valence eigenstates. Fig. 6 d) illustrates the anisotropic d-wave spin texture of the valence band across the Brillouin zone, where the spin orientation varies in a $\mathcal{C}_{4z}\mathbb{T}$ symmetry shape. Note the presence of an internal ring band inversion in the spin-resolved band structure, which is consistent with the predictions of the $\mathcal{C}_{4z}\mathbb{T}$ Hamiltonian model introduced previously in Eqn. (22). These results establish monolayer FeSe as a prototypical topological altermagnet, where d-wave spin splitting and quantized spin transport converge in a realistic 2D-dimensional material.

III. CONCLUSIONS

The combination of rotational symmetries with time-reversal operations provides a framework for engineering topological phases in magnetic materials. By designing low-energy Hamiltonians with preserved $\mathcal{C}_{4z}\mathbb{T}$ and $\mathcal{C}_{3z}\mathbb{T}$ symmetries, we have demonstrated that nontrivial topological phases in 2D and 3D can be protected by these symmetries and characterized by spin Chern numbers, as predicted through K-theory analysis. Our findings show that altermagnetic systems, which exhibit non-relativistic spin splitting in the absence of net magnetization, can support topological phenomena, including symmetry-protected surface, hinge and corner states. These boundary states can be manipulated with the local magnetic moments, represented by the M_0 term in the Hamiltonian. We have also proposed the FeSe monolayer as a realistic candidate for the experimental realization of 2D topological altermagnetic phases. This material can be classified as a d-wave altermagnetic materials with quantized spin Hall conductivity, where the topological phase is protected by $\mathcal{C}_{4z}\mathbb{T}$. Understanding topological altermagnets opens new pathways for spintronic technologies by connecting topological quantum effects with magnetic symmetries.

[1] Šmejkal, L., González-Hernández, R., Jungwirth, T. & Sinova, J. Crystal time-reversal symmetry breaking and spontaneous hall effect in collinear antiferromagnets. *Science Advances* **6**, eaaz8809 (2020). URL https://www.science.org/doi/abs/10.1126/sciadv.aaz8809. https://www.science.org/doi/pdf/10.1126/sciadv.aaz8809.

[2] Šmejkal, L., Sinova, J. & Jungwirth, T. Emerging research landscape of altermagnetism. *Phys. Rev. X* **12**, 040501 (2022). URL https://link.aps.org/doi/10.1103/PhysRevX.12.040501.

[3] Šmejkal, L., Sinova, J. & Jungwirth, T. Beyond conventional ferromagnetism and antiferromagnetism: A phase with nonrelativistic spin and crystal rotation symmetry. *Phys. Rev. X* **12**, 031042 (2022). URL https://link.aps.org/doi/10.1103/PhysRevX.12.031042.

[4] Mazin, I. I., Koepernik, K., Johannes, M. D., González-Hernández, R. & Šmejkal, L. Prediction of unconventional magnetism in doped fesb¡sub¿2¡/sub¿. *Proceedings of the National Academy of Sciences* **118**, e2108924118 (2021). URL https://www.pnas.org/doi/abs/10.1073/pnas.2108924118.

https://www.pnas.org/doi/pdf/10.1073/pnas.2108924118.

[5] Šmejkal, L., MacDonald, A. H., Sinova, J., Nakatsuji, S. & Jungwirth, T. Anomalous hall antiferromagnets. *Nature Reviews Materials* **7**, 482–496 (2022). URL https://doi.org/10.1038/s41578-022-00430-3.

[6] Bai, L. *et al.* Altermagnetism: Exploring new frontiers in magnetism and spintronics. *Advanced Functional Materials* **34**, 2409327 (2024). URL https://advanced.onlinelibrary.wiley.com/doi/abs/10.1002/adfm.202409327. https://advanced.onlinelibrary.wiley.com/doi/pdf/10.1002/adfm.202409327.

[7] Jiang, B. *et al.* Discovery of a metallic room-temperature d-wave altermagnet kv2se2o (2024). URL https://arxiv.org/abs/2408.00320. 2408.00320.

[8] Chen, X. *et al.* Enumeration and representation theory of spin space groups. *Phys. Rev. X* **14**, 031038 (2024). URL https://link.aps.org/doi/10.1103/PhysRevX.14.031038.

[9] Xiao, Z., Zhao, J., Li, Y., Shindou, R. & Song, Z.-D. Spin space groups: Full classification and applications. *Phys. Rev. X* **14**, 031037 (2024). URL https://link.aps.org/doi/10.1103/PhysRevX.14.031037.

[10] Jungwirth, T. *et al.* Altermagnetism: An unconventional spin-ordered phase of matter. *Newton* (2025). URL https://doi.org/10.1016/j.newton.2025.100162.

[11] Gonzalez Betancourt, R. D. *et al.* Spontaneous anomalous hall effect arising from an unconventional compensated magnetic phase in a semiconductor. *Phys. Rev. Lett.* **130**, 036702 (2023). URL https://link.aps.org/doi/10.1103/PhysRevLett.130.036702.

[12] Krempaský, J. *et al.* Altermagnetic lifting of kramers spin degeneracy. *Nature* **626**, 517–522 (2024). URL https://doi.org/10.1038/s41586-023-06907-7.

[13] Gonzalez Betancourt, R. D. *et al.* Anisotropic magnetoresistance in altermagnetic MnTe. *npj Spintronics* **2**, 45 (2024). URL https://doi.org/10.1038/s44306-024-00046-z.

[14] Lee, S. *et al.* Broken kramers degeneracy in altermagnetic mnte. *Phys. Rev. Lett.* **132**, 036702 (2024). URL https://link.aps.org/doi/10.1103/PhysRevLett.132.036702.

[15] Reimers, S. *et al.* Direct observation of altermagnetic band splitting in CrSb thin films. *Nature Communications* **15**, 2116 (2024). URL https://doi.org/10.1038/s41467-024-46476-5.

[16] Lu, W. *et al.* Observation of surface fermi arcs in altermagnetic weyl semimetal crsb (2024). URL https://arxiv.org/abs/2407.13497. 2407.13497.

[17] Zeng, M. *et al.* Observation of spin splitting in room-temperature metallic antiferromagnet crsb. *Advanced Science* **11**, 2406529 (2024). URL https://advanced.onlinelibrary.wiley.com/doi/abs/10.1002/advs.202406529. https://advanced.onlinelibrary.wiley.com/doi/pdf/10.1002/advs.202406529.

[18] Lu, W. *et al.* Signature of topological surface bands in altermagnetic weyl semimetal crsb. *Nano Letters* **25**, 7343–7350 (2025). URL https://doi.org/10.1021/acs.nanolett.5c00482.

[19] Reichlova, H. *et al.* Observation of a spontaneous anomalous hall response in the mn5si3 d-wave altermagnet candidate. *Nature Communications* **15**, 4961 (2024). URL https://doi.org/10.1038/s41467-024-48493-w.

[20] Leiviskä, M. *et al.* Anisotropy of the anomalous hall effect in thin films of the altermagnet candidate mn$_5$si$_3$. *Phys. Rev. B* **109**, 224430 (2024). URL https://link.aps.org/doi/10.1103/PhysRevB.109.224430.

[21] Rial, J. *et al.* Altermagnetic variants in thin films of Mn$_5$Si$_3$. *Phys. Rev. B* **110**, L220411 (2024). URL https://link.aps.org/doi/10.1103/PhysRevB.110.L220411.

[22] Badura, A. *et al.* Observation of the anomalous nernst effect in altermagnetic candidate mn5si3 (2024). URL https://arxiv.org/abs/2403.12929. 2403.12929.

[23] Hasan, M. Z. & Kane, C. L. Colloquium: Topological insulators. *Reviews of Modern Physics* **82**, 3045 (2010). URL https://link.aps.org/doi/10.1103/RevModPhys.82.3045.

[24] Qi, X.-L. & Zhang, S.-C. Topological insulators and superconductors. *Review of Modern Physics* **83**, 1057–1110 (2011). URL https://link.aps.org/doi/10.1103/RevModPhys.83.1057.

[25] Chiu, C.-K., Teo, J. C. Y., Schnyder, A. P. & Ryu, S. Classification of topological quantum matter with symmetries. *Rev. Mod. Phys.* **88**, 035005 (2016). URL https://link.aps.org/doi/10.1103/RevModPhys.88.035005.

[26] Moessner, R. & Moore, J. E. *Topological phases of matter* (Cambridge University Press, 2021).

[27] Kane, C. L. & Mele, E. J. Z$_2$ topological order and the quantum spin hall effect. *Phys. Rev. Lett.* **95**, 146802 (2005). URL https://link.aps.org/doi/10.1103/PhysRevLett.95.146802.

[28] Sheng, D. N., Weng, Z. Y., Sheng, L. & Haldane, F. D. M. Quantum spin-hall effect and topologically invariant chern numbers. *Phys. Rev. Lett.* **97**, 036808 (2006). URL https://link.aps.org/doi/10.1103/PhysRevLett.97.036808.

[29] Fu, L. & Kane, C. L. Time reversal polarization and a z$_2$ adiabatic spin pump. *Phys. Rev. B* **74**, 195312 (2006). URL https://link.aps.org/doi/10.1103/PhysRevB.74.195312.

[30] Fu, L., Kane, C. L. & Mele, E. J. Topological insulators in three dimensions. *Phys. Rev. Lett.* **98**, 106803 (2007). URL https://link.aps.org/doi/10.1103/PhysRevLett.98.106803.

[31] Prodan, E. Robustness of the spin-chern number. *Phys. Rev. B* **80**, 125327 (2009). URL https://link.aps.org/doi/10.1103/PhysRevB.80.125327.

[32] Lin, K.-S. *et al.* Spin-resolved topology and partial axion angles in three-dimensional insulators. *Nature Communications* **15**, 550 (2024). URL https://doi.org/10.1038/s41467-024-44762-w.

[33] González-Hernández, R. & Uribe, B. Spin weyl topological insulators. *Phys. Rev. B* **109**, 045126 (2024). URL https://link.aps.org/doi/10.1103/PhysRevB.109.045126.

[34] Lange, G. F., Bouhon, A. & Slager, R.-J. Spin texture as a bulk indicator of fragile topology. *Phys. Rev. Res.* **5**, 033013 (2023). URL https://link.aps.org/doi/10.1103/PhysRevResearch.5.033013.

[35] González-Hernández, R., Serrano, H. & Uribe, B. Spin chern number in altermagnets. *Phys. Rev. B* **111**, 085127 (2025). URL https://link.aps.org/doi/10.1103/PhysRevB.111.085127.

[36] Zhu, D., Zhuang, Z.-Y., Wu, Z. & Yan, Z. Topological superconductivity in two-dimensional altermagnetic metals. *Phys. Rev. B* **108**, 184505 (2023). URL https://link.aps.org/doi/10.1103/PhysRevB.108.184505.

[37] Ghorashi, S. A. A., Hughes, T. L. & Cano, J. Altermagnetic routes to majorana modes in zero net magnetiza-

tion. *Phys. Rev. Lett.* **133**, 106601 (2024). URL https://link.aps.org/doi/10.1103/PhysRevLett.133.106601.

[38] Ma, H.-Y. & Jia, J.-F. Altermagnetic topological insulator and the selection rules. *Phys. Rev. B* **110**, 064426 (2024). URL https://link.aps.org/doi/10.1103/PhysRevB.110.064426.

[39] Li, Y.-Y. & Zhang, S.-B. Floating edge bands in the bernevig-hughes-zhang model with altermagnetism. *Phys. Rev. B* **111**, 045106 (2025). URL https://link.aps.org/doi/10.1103/PhysRevB.111.045106.

[40] Wan, Y.-H. & Sun, Q.-F. Altermagnetism-induced parity anomaly in weak topological insulators. *Phys. Rev. B* **111**, 045407 (2025). URL https://link.aps.org/doi/10.1103/PhysRevB.111.045407.

[41] Heinsdorf, N. Altermagnetic instabilities from quantum geometry. *Phys. Rev. B* **111**, 174407 (2025). URL https://link.aps.org/doi/10.1103/PhysRevB.111.174407.

[42] Li, Z., Li, Z. & Qiao, Z. Altermagnetism-induced topological phase transitions in the kane-mele model. *Phys. Rev. B* **111**, 155303 (2025). URL https://link.aps.org/doi/10.1103/PhysRevB.111.155303.

[43] Zhang, M.-H., Xiao, L. & Yao, D.-X. Topological magnons in a collinear altermagnet (2025). URL https://arxiv.org/abs/2407.18379. 2407.18379.

[44] Fernandes, R. M., de Carvalho, V. S., Birol, T. & Pereira, R. G. Topological transition from nodal to nodeless zeeman splitting in altermagnets. *Phys. Rev. B* **109**, 024404 (2024). URL https://link.aps.org/doi/10.1103/PhysRevB.109.024404.

[45] Ma, H.-Y. & Jia, J.-F. Altermagnetic topological insulator with $\mathcal{C}$-paired spin-valley locking. *Quantum Frontiers* **3**, 22 (2024). URL https://doi.org/10.1007/s44214-024-00070-4.

[46] Parshukov, K., Wiedmann, R. & Schnyder, A. P. Topological crossings in two-dimensional altermagnets: Symmetry classification and topological responses. *Phys. Rev. B* **111**, 224406 (2025). URL https://link.aps.org/doi/10.1103/PhysRevB.111.224406.

[47] Dürrnagel, M. *et al.* Altermagnetic phase transition in a lieb metal. *Phys. Rev. Lett.* **135**, 036502 (2025). URL https://link.aps.org/doi/10.1103/2g3v-z76q.

[48] He, T. *et al.* Quasi-one-dimensional spin transport in altermagnetic Z^3 nodal net metals. *Phys. Rev. Lett.* **133**, 146602 (2024). URL https://link.aps.org/doi/10.1103/PhysRevLett.133.146602.

[49] Zou, J.-Y., Fu, B. & Shen, S.-Q. Topological properties of c4zt-symmetric semimetals. *Communications Physics* **7**, 275 (2024). URL https://doi.org/10.1038/s42005-024-01767-7.

[50] Farajollahpour, T., Ganesh, R. & Samokhin, K. V. Berry curvature-induced transport signature for altermagnetic order. *npj Quantum Materials* **10**, 77 (2025). URL https://doi.org/10.1038/s41535-025-00805-z.

[51] Meng-Han, Z., Xuan, G. & Yao, D.-X. Dirac points and weyl phase in a honeycomb altermagnet (2025). URL https://arxiv.org/abs/2412.03657. 2412.03657.

[52] Day, I. A., Varentcova, A., Varjas, D. & Akhmerov, A. R. Pfaffian invariant identifies magnetic obstructed atomic insulators. *SciPost Phys.* **15**, 114 (2023). URL https://scipost.org/10.21468/SciPostPhys.15.3.114.

[53] Bernevig, B. A., Hughes, T. L. & Zhang, S.-C. Quantum spin hall effect and topological phase transition in hgte quantum wells. *Science* **314**, 1757–1761 (2006). URL https://www.science.org/doi/abs/10.1126/science.1133734. https://www.science.org/doi/pdf/10.1126/science.1133734.

[54] Serrano, H., Uribe, B. & Xicoténcatl, M. A. Magnetic equivariant k-theory (2025). URL https://arxiv.org/abs/2503.06267. 2503.06267.

[55] Schindler, F. *et al.* Higher-order topological insulators. *Science Advances* **4**, eaat0346 (2018). URL https://www.science.org/doi/abs/10.1126/sciadv.aat0346.

[56] Ojito, D. P., Prodan, E. & Stoiber, T. C*-framework for higher-order bulk-boundary correspondences (2024). URL https://arxiv.org/abs/2406.04226. 2406.04226.

[57] Li, Y.-X., Liu, Y. & Liu, C.-C. Creation and manipulation of higher-order topological states by altermagnets. *Phys. Rev. B* **109**, L201109 (2024). URL https://link.aps.org/doi/10.1103/PhysRevB.109.L201109.

[58] Serrano, H., Uribe, B. & Xicoténcatl, M. A. Rational magnetic equivariant K-theory. *Rev. Acad. Colombiana Cienc. Exact. Fís. Natur.* **49**, 183–197 (2025).

[59] Nekrasov, I. A., Pavlov, N. S., Sadovskii, M. V. & Slobodchikov, A. A. Electronic structure of fese monolayer superconductors. *Low Temperature Physics* **42**, 891–899 (2016). URL https://doi.org/10.1063/1.4965892. https://pubs.aip.org/aip/ltp/article-pdf/42/10/891/14844719/891_1_online.pdf.

[60] Liu, K., Lu, Z.-Y. & Xiang, T. Atomic and electronic structures of fese monolayer and bilayer thin films on srtio$_3$ (001): First-principles study. *Phys. Rev. B* **85**, 235123 (2012). URL https://link.aps.org/doi/10.1103/PhysRevB.85.235123.

[61] Liu, D. *et al.* Electronic origin of high-temperature superconductivity in single-layer fese superconductor. *Nature Communications* **3**, 931 (2012). URL https://doi.org/10.1038/ncomms1946.

[62] Kitamura, T., Yamashita, T., Ishizuka, J., Daido, A. & Yanase, Y. Superconductivity in monolayer fese enhanced by quantum geometry. *Phys. Rev. Res.* **4**, 023232 (2022). URL https://link.aps.org/doi/10.1103/PhysRevResearch.4.023232.

[63] Mazin, I., González-Hernández, R. & Šmejkal, L. Induced monolayer altermagnetism in MnP(S,Se)$_3$ and FeSe (2023). URL https://arxiv.org/abs/2309.02355. 2309.02355.

[64] Zheng, F., Wang, Z., Kang, W. & Zhang, P. Antiferromagnetic fese monolayer on srtio3: The charge doping and electric field effects. *Scientific Reports* **3**, 2213 (2013). URL https://doi.org/10.1038/srep02213.

[65] Tan, S. *et al.* Interface-induced superconductivity and strain-dependent spin density waves in fese/srtio3 thin films. *Nature Materials* **12**, 634–640 (2013). URL https://doi.org/10.1038/nmat3654.